Quality Assessment of HF Radar–Derived Surface Currents Using Optimal Interpolation

YING-CHIH FANG, THOMAS J. WEINGARTNER, RACHEL A. POTTER, PETER R. WINSOR, AND HANK STATSCEWICH

School of Fisheries and Ocean Sciences, University of Alaska Fairbanks, Fairbanks, Alaska

(Manuscript received 4 June 2014, in final form 18 September 2014)

ABSTRACT

This study investigates the applicability of the optimal interpolation (OI) method proposed by Kim et al. for estimating ocean surface currents from high-frequency radar (HFR) in the northeastern Chukchi Sea, where HFR siting is dictated by power availability rather than optimal locations. Although the OI technique improves data coverage when compared to the conventional unweighted least squares fit (UWLS) method, biased solutions can emerge. The quality of the HFR velocity estimates derived by OI is controlled by three factors: 1) the number of available incorporating radials (AR), 2) the ratio of the incorporating radials from multiple contributing site locations [ratio of overlapping radial velocities (ROR) or radar geometry], and 3) the positive definiteness [condition number (CN)] of the correlation matrix. Operationally, ROR does not require knowledge of the angle covariance matrix used to compute the geometric dilution of precision (GDOP) in the UWLS method and can be computed before site selection to optimize coverage or after data processing to assess data quality when applying the OI method. The Kim et al. method is extended to examine sensitivities to data gaps in the radial distribution and the effects on OI estimates.

1. Introduction

Ocean surface currents can be mapped over broad areas from a shore-based high-frequency radar (HFR) array. In real-time applications, HFRs can support search and rescue missions, identify oil spill trajectories, and guide adaptive sampling. Each radar receives Doppler-shifted signals that are Bragg scattered from surface gravity waves one-half the wavelength of the transmitted radar wave (Crombie 1955). Because it is induced by the current upon which the surface gravity waves propagate, this Doppler shift is used to calculate surface velocity. The velocity is then projected onto a spoke pattern originating from each HFR field site, resulting in a map of one-dimensional surface current measurements advancing or retreating from each site. Such quantities are referred to as the radial velocity components $\mathbf{r}$ or radials, where $\mathbf{r}(\mathbf{x}, t) = \mathbf{u}(\mathbf{x}, t) \cdot \hat{\mathbf{x}}_\mathbf{r}$. The surface current vector $\mathbf{u}(\mathbf{x}, t) = (u, v)$ represents the east–west (u) and north–south (v) velocity components; $\mathbf{x} = (x, y)$ is the corresponding coordinate system; t is the time step when $\mathbf{r}$ is measured; and $\hat{\mathbf{x}}_\mathbf{r}$ is a unit vector aligned from $\mathbf{x}$ to the location of the HFR. For a direction-finding HFR, such as the SeaSonde system manufactured by CODAR Ocean Sensors, $\mathbf{r}$ are measured in angular sectors divided by concentric rings originating from the HFR (Lipa and Barrick 1983; Gurgel 1994). Multiple HFR are required to resolve the two-dimensional $\mathbf{u}$, estimated by incorporating all $\mathbf{r}$ within a specified search radius (d_o) surrounding $\mathbf{x}$. Several methods have been designed to resolve $\mathbf{u}$ from HFR measurements. Among them, the unweighted least squares fit (UWLS) method is widely used throughout the HFR community and is the default method applied by SeaSonde processing software.

One quality assessment commonly used with the UWLS method is the geometric dilution of precision (GDOP) error (Chapman et al. 1997; Barrick 2006). GDOP is computed by inverting the angle covariance matrix and is a function of the number of measurements available and the distance between HFR. For two 5-MHz SeaSonde systems having a range of ~180 km, the GDOP threshold excludes $\hat{\mathbf{x}}_\mathbf{r}$ with intersecting angles between $\mathbf{r}$ of $<15°$. Utilizing GDOP, optimal HFR site

Corresponding author address: Ying-Chih Fang, School of Fisheries and Ocean Sciences, University of Alaska Fairbanks, P.O. Box 757220, Fairbanks, AK 99775-7220.
E-mail: yfang2@alaska.edu

DOI: 10.1175/JTECH-D-14-00109.1

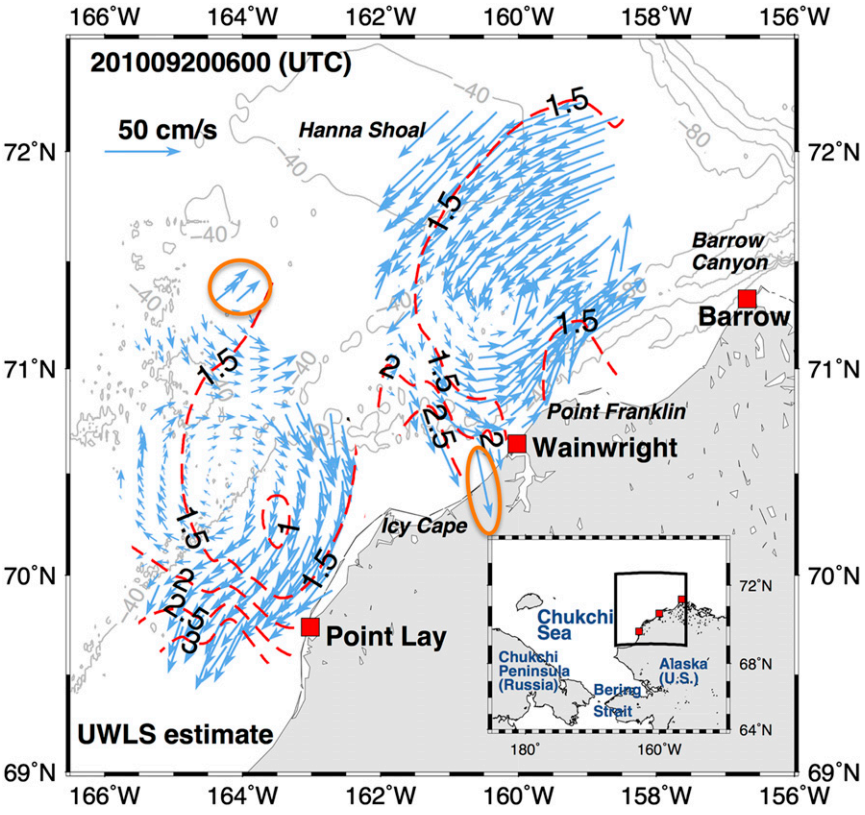

FIG. 1. Surface currents at 0600 UTC 20 Sep 2010 mapped by the Chukchi Sea HFR array (red squares) using the UWLS method. Orange circles highlight current solutions with high GDOP (red dashed contours). Gray contours indicate bathymetry at 40-m intervals. For clarity, only subsampled vectors are shown.

spacing is found to be ~76 km. If HFR spacing is nonoptimal, then the distribution of **u** will be reduced. One goal of this paper is to evaluate **u** under such circumstances.

In 2010 and 2011, three 5-MHz (25-kHz bandwidth) SeaSonde systems were deployed along the northwestern Alaskan coast in the villages of Barrow, Wainwright, and Point Lay to map surface currents during the late July–early November ice-free season in the northeastern Chukchi Sea (Fig. 1). This HFR array provided near-real-time measurements of surface currents and yielded unprecedented data coverage in this region (the radar mask).

The Chukchi HFR sites had limitations—these were the only locations along this coast with an electrical grid. Thus, optimal site spacing was not possible, and the HFR placement was dictated by power availability. The distance between each HFR site was ~150 km, nearly twice the optimal site spacing. Moreover, the coastline geometry of Icy Cape and Point Franklin blocked signal propagation. In aggregate these limitations resulted in the radar mask being split into two regions separated by a persistent data gap north of Icy Cape (Fig. 1).

Spurious **u** are often found near the boundary of the radar mask (Fig. 1, orange circles) and are denoted by large velocities, veer relative to neighboring **u**, and occur in regions of high GDOP. Additionally, **r** may be noisy due to environmental conditions or ionospheric interference. Nightly reflections of the HFR signal from the ionosphere lower the signal-to-noise ratio in radar spectral returns at ranges of more than 90 km, thus reducing the effective range of each system (Teague 2001). Figure 2 shows the average HFR data returns per hour of day by examining the return spectra following Fang et al. (2011). Data returns diminish for ~5 h daily, typically between 0700 and 1100 UTC. Ionospheric interference is persistent along high-latitude coasts and is also encountered at lower-latitude HFR sites.

The UWLS method assumes infinite signal and unit error variances, such that each of the **r** incorporated into the estimate of **u** are treated identically. Thus, this approach is highly sensitive to outliers. To mitigate the influence of noise and enhance confidence in velocity estimates within the radar mask, we investigate the applicability of the optimal interpolation (OI) method

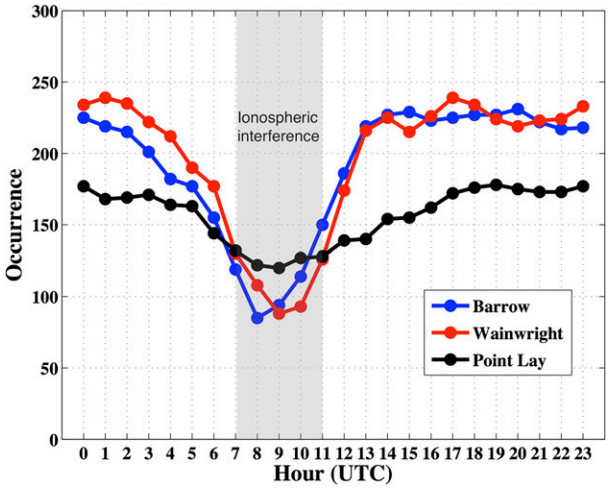

FIG. 2. Average number of 2010 HFR data returns per hour of day for Barrow (blue), Wainwright (red), and Point Lay (black). Shaded area indicates the period of ionospheric interference. Similar results were found for 2011.

(Kim et al. 2007, 2008) to the Chukchi Sea HFR array. Comparing OI- and UWLS-estimated **u**, we found that the magnitudes of the current vectors are similar in their spatial distributions, but in some portions of the radar mask, the directions of the UWLS- and OI-derived vectors differed noticeably from one another. We explore the reasons for these differences.

OI has been implemented in Southern California and the Mid-Atlantic Bight (Kim et al. 2007, 2008; Kohut et al. 2012). Kohut et al. (2012) evaluated the OI and UWLS methods by comparing **u** with in situ data. Their results, and those of Kim et al. (2008), indicate that OI-derived currents reduce noise and yield fewer spurious vector solutions than those obtained from the UWLS method. However, Kohut et al. (2012) only evaluated specific grid points within the radar mask, which, while showing favorable results, did not reveal potential limitations of the OI method.

This study is an attempt to better quantify the limitations of the OI method that, when understood, enhance the ability to analyze HFR datasets. Using a series of simulations designed to assess the capabilities of the OI method, to diagnose parameter selections, and to provide insight into how to better interpret radar-estimated **u**, we find that the ratio of contributing **r** from each HFR site can serve as a proxy for the estimated data quality and can be used to optimize HFR site selection.

The paper is arranged as follows: Background information on HFR data acquisition and processing is discussed in section 2. A brief review of the OI method developed by Kim et al. (2007, 2008) and its implementation are given in section 3. Section 4 provides an assessment of the OI method. A discussion and summary complete the paper.

2. Ocean surface current observations in the northeastern Chukchi Sea

The shallow (~50 m) Chukchi Sea connects the Arctic and Pacific Oceans via the Bering Strait. The shelf circulation is forced by the large-scale pressure gradient between these two basins and is nominally northward and guided by the bathymetry (Winsor and Chapman 2004; Weingartner et al. 2005). Within the radar mask, flow typically includes the swift (~0.5–1.0 m s^{-1}) Alaskan Coastal Current (ACC), which is a coastal jet flowing northeastward within ~40 km of the coast between Wainwright and Barrow (Paquette and Bourke 1974). Over the shelf south of Hanna Shoal, flow is weaker and broader and transports central shelf waters eastward toward Wainwright and the head of Barrow Canyon (Fig. 1). On average, the flow between Barrow Canyon and Hanna Shoal is very weak. Wind-forced reversals of the ACC and shelf flow are very common and may last for several days to weeks (Weingartner et al. 1999, 2005).

Our SeaSonde systems collected **r** at 30-min intervals over an effective depth of ~2 m (Stewart and Joy 1974) and had a resolution in range and bearing of 6 km and 5°, respectively. All spectra acquired in a 3-h window were averaged to produce an hourly **r** file. Antennas were calibrated using a beam-pattern measurement to improve the direction-finding capability of the receive antenna in the local environment (Barrick and Lipa 1986). Subsequent to acquisition, cross spectra were visually inspected to ensure software parameters were optimized for locating Bragg peaks at each site throughout the field season. The **r** were further quality controlled by removing $\mathbf{r} > 150$ cm s^{-1}, **x** with less than 10% coverage, and velocities exceeding three standard deviations from the temporal mean of each **x**. HFR_Progs (https://cencalarchive.org/~cocmpmb/COCMP-wiki/) was used to distribute **r** onto uniform grid points (Fig. 3). If multiple contributing sites provide at least three available **r** in the d_o, then these **r** are then used to estimate **u** through the UWLS and OI methods at each **x**. Every hour, 90 min of **r** before and after the cardinal hour are averaged to produce a map of **u** by each method. For the UWLS method, d_o is defined as 12 km, whereas the d_o for the OI method is 35 km, with this choice discussed in section 3. In the UWLS procedure, choosing a d_o too large results in **r** far from the grid point of interest having a large influence on the estimated **u**. In the OI method **r** are weighted with respect to their distance from the grid point of the resulting **u** and thus utilize a larger d_o. These weighting schemes are a key difference between the two methods.

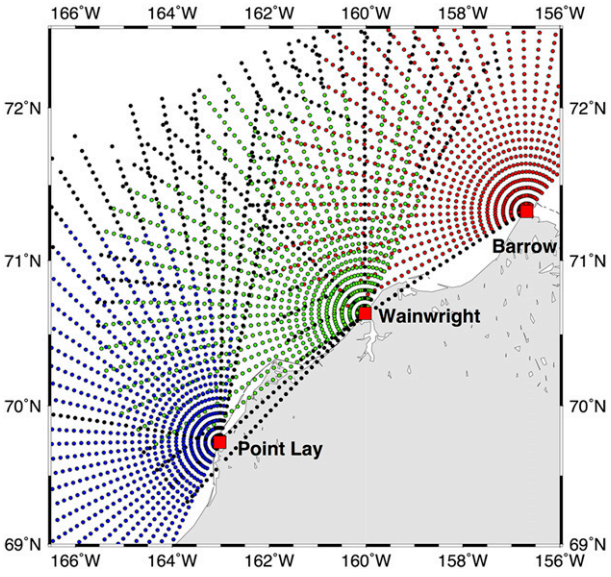

FIG. 3. Grid points of radial velocities measured by the HFR in Barrow (red), Wainwright (green), and Point Lay (blue) during the 2010 operating season. Black dots indicate grid points that were removed from the dataset during the initial QA/QC process.

HFR data from 2010 (September–October) and 2011 (August–October) are used in this paper with the main analysis based on the former. The 2011 data are used to compute related parameters of the OI method for comparison purposes.

3. Optimal interpolation

a. Objective analysis

For HFR data, $\mathbf{u}$ and $\mathbf{r}$ have the following relationship:

$$\mathbf{r} = \mathbf{g}^{\mathrm{T}}\mathbf{u} + \mathbf{n}, \tag{1}$$

where $\mathbf{g}$ is the angle matrix ($\mathbf{g}(\mathbf{x}) = [\cos\theta\ \sin\theta]$, with θ as the bearing at $\mathbf{x}$ measured counterclockwise from east), and $\mathbf{n}$ is the error matrix. In the UWLS method, $(\mathbf{g}^{\mathrm{T}}\mathbf{g})^{-1}$ is the inverse of the angle covariance matrix, where superscripts "T" and "−1" denote the matrix transpose and inverse, respectively. The norm of $(\mathbf{g}^{\mathrm{T}}\mathbf{g})^{-1}$ (calculated within the HFR_Progs toolbox) is the GDOP. Based on the Gauss–Markov theorem, unknown $\mathbf{u}$ with a minimum variance from observation $\mathbf{r}$ can be written as

$$\mathbf{u} = \mathbf{cov}_{dm}^{\mathrm{T}}\,\mathbf{cov}_{dd}^{-1}\mathbf{r}, \tag{2}$$

where $\mathbf{cov}_{dm}$ is the covariance matrix between the $\mathbf{u}$ and $\mathbf{r}$, and $\mathbf{cov}_{dd}$ represents the covariance matrix among $\mathbf{r}$. Assuming that $\mathbf{r}$ and $\mathbf{n}$ and $\mathbf{u}$ and $\mathbf{n}$ are uncorrelated implies that

$$(\mathbf{cov}_{dm})_{ik} = \langle \mathbf{r}_i\mathbf{u}_k^{\mathrm{T}}\rangle, \tag{3}$$

$$(\mathbf{cov}_{dd})_{ij} = \langle \mathbf{r}_i\mathbf{r}_j^{\mathrm{T}}\rangle + \langle \mathbf{n}_i\mathbf{n}_j^{\mathrm{T}}\rangle, \tag{4}$$

where i and j represent the different grid points of $\mathbf{r}$, k indicates the grid point of $\mathbf{u}$, $\langle \mathbf{n}_i\mathbf{n}_j^{\mathrm{T}}\rangle$ denotes the error covariance matrix, and $\langle\cdot\rangle$ is the expected value operator. The error covariance matrix is assumed to be

$$\langle \mathbf{n}_i\mathbf{n}_j^{\mathrm{T}}\rangle = \sigma_r^2\mathbf{I}, \tag{5}$$

where $\mathbf{I}$ is the identity matrix, and σ_r^2 is the noise variance of $\mathbf{r}$. From (1), (3), and (4), the covariance matrix can be written as

$$(\mathbf{cov}_{dm})_{ik} = \mathbf{g}_i^{\mathrm{T}}\langle \mathbf{u}_i\mathbf{u}_k^{\mathrm{T}}\rangle \tag{6}$$

$$(\mathbf{cov}_{dd})_{ij} = \mathbf{g}_i^{\mathrm{T}}\langle \mathbf{u}_i\mathbf{u}_j^{\mathrm{T}}\rangle\mathbf{g}_j + \sigma_r^2\mathbf{I}. \tag{7}$$

Kim et al. (2007) express the covariance matrix for $\mathbf{u}$ in terms of the correlation and variance:

$$\langle \mathbf{u}_i\mathbf{u}_k^{\mathrm{T}}\rangle = \sigma_s^2(\mathbf{x}_k)\mathbf{I}\rho(\Delta\mathbf{x}_{ik}) \tag{8}$$

$$\langle \mathbf{u}_i\mathbf{u}_j^{\mathrm{T}}\rangle = \sigma_s^2(\mathbf{x}_k)\mathbf{I}\rho(\Delta\mathbf{x}_{ij}), \tag{9}$$

where $\sigma_s^2(\mathbf{x}_k)$ is the signal variance of $\mathbf{u}$ at the grid points $\mathbf{x}_k$, $\rho(\Delta\mathbf{x}_{ik})$ is the spatial correlation function between $\mathbf{x}_i$ (the grid points of $\mathbf{r}_i$) and $\mathbf{x}_k$ (the grid points of $\mathbf{u}_k$), and Δ is the distance between these grid points. Note that (9) is similar to (8) and that (9) is the spatial correlation function for grid points of $\mathbf{r}$ at $\mathbf{x}_i$ and $\mathbf{x}_j$. Kim et al. (2008) define the spatial correlation function to be

$$\rho(\Delta\mathbf{x}) = \exp\left[-\sqrt{\left(\frac{\Delta x}{\lambda_x}\right)^2 + \left(\frac{\Delta y}{\lambda_y}\right)^2}\right], \tag{10}$$

where λ_x and λ_y are the decorrelation length scales in the x and y directions, respectively. These length scales are discussed in the following section.

b. Setting the parameters of OI

1) SIGNAL AND ERROR VARIANCES

The covariance matrices require a priori knowledge of σ_s^2 and σ_r^2. Following Kim et al. (2008) and Kohut et al. (2012), we determine these parameters by calculating standard deviations of the measured $\mathbf{r}$. For the measured $\mathbf{r}$ from Barrow, Wainwright, and Point Lay HFR in 2010, the standard deviations are 21.68, 17.87, and 6.39 cm s^{-1}, respectively, with an average value of ~15 cm s^{-1}. We doubled the standard deviation to ensure it was not underestimated, resulting in σ_s^2 equal to 900 cm^2 s^{-2}. An

examination of other assumed σ_s^2 values (e.g., 200, 500, 1500 $\mathrm{cm^2\,s^{-2}}$) indicated that the OI results were largely insensitive to our choices.

The error variance (σ_r^2) is attributed to measurement uncertainties. Liu et al. (2010) found the root-mean-square (RMS) difference ranged from 6 to 10 $\mathrm{cm\,s^{-1}}$ for hourly **r** for 5-MHz SeaSonde systems. Lipa (2003) found that the RMS difference converged to 10 $\mathrm{cm\,s^{-1}}$, although that estimate was based on 25-MHz systems. We chose an RMS difference of 10 $\mathrm{cm\,s^{-1}}$ as a reasonable estimate of the measurement uncertainties for our sites and set σ_r^2 to 100 $\mathrm{cm^2\,s^{-2}}$ in (5). This estimate is 3 times larger than that of Kim et al. (2008), who used OI on 25-MHz systems. The larger error variance leads to smoother estimates, suppresses noise, and is chosen as reasonable in our study domain.

2) Decorrelation length scale and search radius

Kim et al. (2008) recommend the decorrelation length scale be within a factor of 4 of the spatial resolution of **u**. Following Kim et al. (2007), we find the range of λ_x to be 21–71 km in 2010 and 18–42 km in 2011, while the ranges for λ_y are 10–15 and 9–11 km. When compared with λ_y, the larger values of λ_x are due to the ACC. The differences between the years could be due to differences in the temporal span (2011 had a longer dataset) and/or because the ACC was more coherent in 2011 than in 2010 (Weingartner et al. 2013). The spatial correlation structure was examined across the ACC near Wainwright by decomposing the radar-estimated **u** (by the UWLS method) into alongshore (56°T) and cross-shore (326°T) velocity components for a 100-km-long transect. Results indicate that the *e*-folding scale of the cross-shore velocity component is larger than the alongshore scale, so the larger λ_x found here is expected.

The values of λ_x or λ_y should not be so large as to include **r** far from the **u** grid point because a value that is too large may oversmooth and blur small-scale variations. Kim et al. (2008) suggested that the calculated decorrelation length scale from the HFR data should be treated as an upper bound. Kohut et al. (2012) showed that the OI estimates were insensitive to changes in the decorrelation length scales. In this analysis λ_x and λ_y were defined as 12 km (twice the spatial resolution) and the same as d_o used in the UWLS method (Fig. 1). We will show that this choice still captures the general circulation pattern of surface currents as detected by the UWLS method. The d_o in OI sets the smallest spatial weighting far from **x** and is defined as d_o = 35 km. Hence, for OI, the spatial correlation weight function decreases to 0.24 at 12 km and to 0.05 at 35 km.

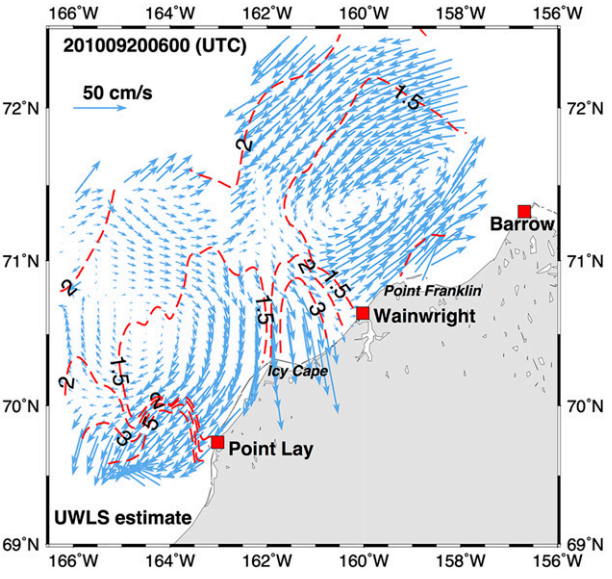

FIG. 4. As in Fig. 1, but using a 35-km search radius. Red dashed contours show corresponding GDOP. For clarity, only subsampled vectors are shown.

c. *Implementing OI*

The OI algorithm (provided by Dr. Sung Yong Kim) works in conjunction with the HFR_Progs toolbox. The first step of the algorithm loads **r** and its corresponding bearing. These bearings comprise the angle matrix **g** and the given σ_s^2 and σ_r^2 variances are constructed as given by (7)–(9). Then the distance ($\Delta\mathbf{x}_{ij}$) between the grid points of $\mathbf{r}_{ij}$, the distance ($\Delta\mathbf{x}_{ik}$) between the grid points of different $\mathbf{r}_i$, and the grid point ($\mathbf{x}_k$) of the estimated $\mathbf{u}_k$ are calculated and used in (8) and (9) to compute the local spatial correlation function. Afterward, the data-model and data–data covariance matrices, (6) and (7), are computed. Finally, the OI-estimated **u** is retrieved from (2).

d. *An example of OI-estimated surface currents and their relationship with GDOP*

Before introducing the OI-estimated **u**, we present a map of **u** estimated by the UWLS method using 35 km for d_o (Fig. 4; chosen at the same hour as in Fig. 1). Although the data gap north of Icy Cape is filled, vector magnitudes in this region are amplified, and the GDOP value is high (~3). This amplification is a typical example of GDOP instability. Vectors are also magnified along the edge of the radar mask due to the equal weighting of **r**. Treating **r** measured 35 and 5 km away from the grid for **u** with the same weight is likely unreasonable.

For the same dataset, an example of OI-estimated **u** is shown in Fig. 5. The OI-estimated **u** fill the gap north of Icy Cape and capture nearly identical features as that in

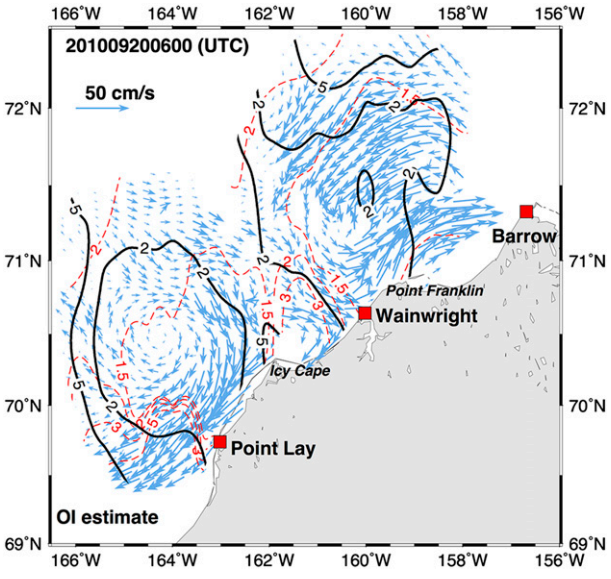

FIG. 5. Surface currents at 0600 UTC 20 Sep 2010 mapped by the Chukchi Sea HFR array (red squares) calculated using the OI method. Red dashed contours show GDOP computed using the UWLS method with a 35-km search radius. Black contours indicate the CN of $\mathbf{cov}_{dm}^{\mathrm{T}}\,\mathbf{cov}_{dd}^{-1}$ (see text). For clarity, only subsampled vectors are shown.

Fig. 1. For example, the eddylike current field northwest of Point Lay is very similar in both methods. However, the amplified vectors seen in Figs. 1 and 4 are not present in the OI estimates of Fig. 5. This is especially true along the boundary of the radar mask because the OI method tapers the solutions toward zero when the number of **r** at a given $\mathbf{x}_k$ is insufficient to estimate $\mathbf{u}_k$ (Kim et al. 2008). Although located in a region of high GDOP, these vectors are not amplified. This suggests that GDOP may not be applicable to the OI method. Instead, we compute the condition number (CN) of $\mathbf{cov}_{dm}^{\mathrm{T}}\,\mathbf{cov}_{dd}^{-1}$ (see section 4), which is a measure of the sensitivity of the inverse of a matrix and reflects how much variation will be brought to **u** from small variations in **r**. In Fig. 5, the radar mask is split into two relatively low CN zones (<2), with high CN zones (>2) found north of Icy Cape and in the outer edges of the radar mask. In aggregate the locations of the tapered vectors within the spatial structure of CN suggest that CN is the OI analog to GDOP used in the UWLS method. Note that the computed CN results from the matrix containing both angles and the correlation function, whereas GDOP is solely from the angle matrix. We will show later that CN is one of the controlling factors for OI estimate quality.

Nevertheless, there are notable differences between the two methods. For example, all surface currents are southwestward in the UWLS estimate north of 72°N, whereas sheared flows are evident in the OI estimate. If the OI method is used to process HFR data, then it is worth determining if such features are reliable. Kim et al. (2008) illustrated the uncertainties of the OI estimates in terms of error ellipses. However, we will show that large and small error ellipses may appear in the same location, thus making interpretation difficult. To examine the source of such discrepancies, we investigate the limitation of (2) using a series of test simulations in section 4.

4. Error analysis

a. *Unidirectional flow field*

1) UNIFORMLY EASTWARD CURRENT

The first test scenario considers a simple flow field of spatially uniform, time-invariant eastward currents of $u = 10\,\mathrm{cm\,s^{-1}}$ and $v = 0\,\mathrm{cm\,s^{-1}}$. This flow field is converted to **r** based on (1) for each of the radial velocity grid points (Fig. 3). The resulting **r** are then used to estimate **u** via the UWLS method (with d_o set to 35 km for comparison) and the OI method described in section 3. Results, shown in Fig. 6a, indicate that the OI-resolved **u** are well determined over most of the radar mask; however, veered vectors, with reduced magnitudes, are found along the boundary of the radar mask and along the baselines between radar sites. The UWLS-resolved **u** are all well determined and unbiased. In other words, in particular regions the OI method produces currents containing north–south velocity components even though the flow is purely eastward. North of the Barrow HFR site [~72°N, ~157°W (region B)], there is a region where the OI-estimated **u** are very weak (Figs. 6b,c). This region is unique because just west of it, the OI-estimated **u** are very nearly eastward. We examine this region in more detail in the following section.

2) UNIFORMLY NORTHWARD CURRENT

In this second scenario, the input flow field has constant and spatially uniform northward currents ($u = 0\,\mathrm{cm\,s^{-1}}$ and $v = 10\,\mathrm{cm\,s^{-1}}$). Following the same procedure as before, the OI-resolved **u** are shown in Fig. 7a. Again, the resulting **u** by the OI method are all reasonable near the center of the radar mask. However, near the boundary of the radar mask and along the radar baselines, the OI method tends to generate east–west velocity components. In contrast, Fig. 6c, which contained very weak **u** for the constant east–west flow case, now has a good estimate (Fig. 7c). Region B is representative of similar regions within the radar mask. Its main characteristic is that it is near the boundary of the radar mask, outside of the limit of **r** coverage by the Wainwright radar; however, **u** are derived in this region due to the large d_o. Note that the UWLS method

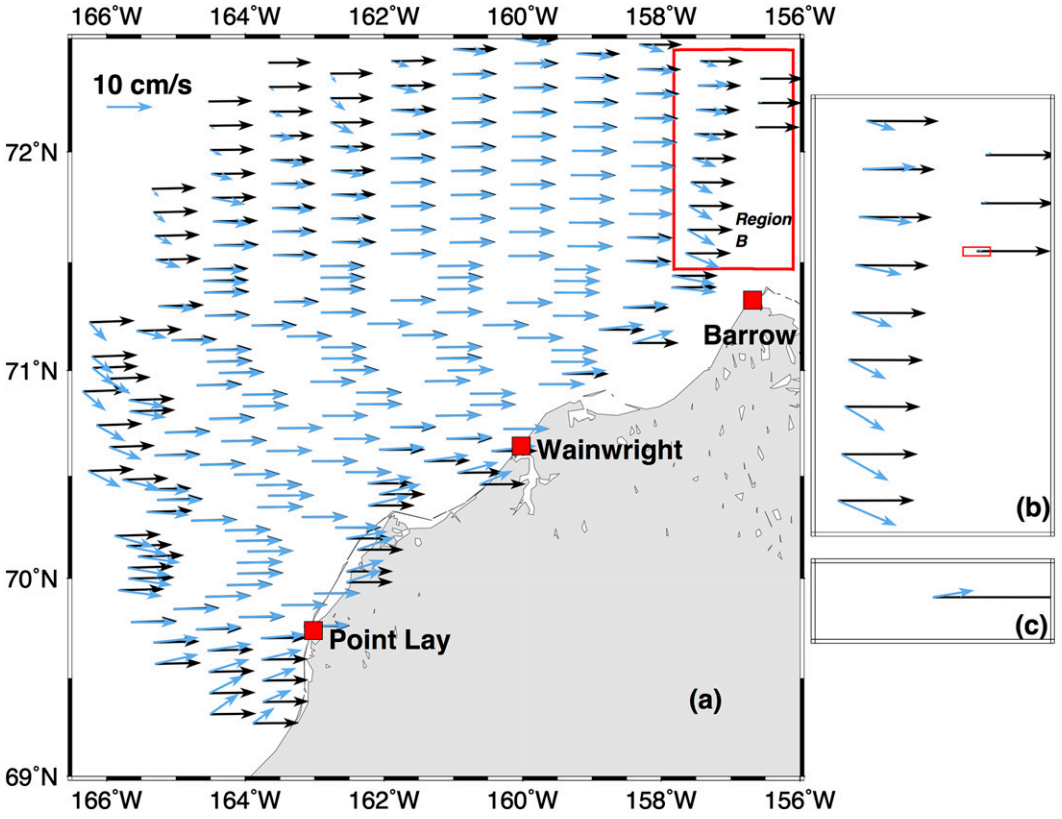

FIG. 6. (a) Example of the OI-estimated (blue) and UWLS-estimated (black) surface currents derived from modeled uniformly eastward currents. OI and UWLS vectors are overlapped. For clarity, only subsampled vectors are shown. Red squares represent locations of HFR. Red rectangle highlights region B. (b) Enlargement of region B. (c) Enlargement to show the detail of the red rectangle area in (b).

provides perfect estimates, even in regions of high GDOP. This suggests UWLS is an unbiased estimator in this modeled flow, where $\mathbf{n} = 0$. However, the estimated $\mathbf{u}$ in region B from the two modeled flows show distinctly different results, indicating OI is a biased estimator due to weighting of $\mathbf{r}$ in d_o.

In region B, the majority of the incorporated $\mathbf{r}$ are from the Barrow HFR and are oriented in an approximately north–south direction. For eastward currents, $\mathbf{r}$ cannot be properly resolved because $\mathbf{u} \cdot \hat{\mathbf{x}}_\mathbf{r} \sim 0$. Although there are those that can be resolved within d_o, they are far away from the grid point of the estimated $\mathbf{u}$. Therefore, these $\mathbf{r}$ have small weight with the result being a biased estimate of $\mathbf{u}$. Conversely, for northward currents, $\mathbf{r}$ can be properly resolved in the OI d_o and produce a valid result. This suggests that in the case of OI, if the majority of the incorporated $\mathbf{r}$ are from a single HFR site, then significant bias errors will be found in estimated $\mathbf{u}$.

Similar experiments were conducted using $(u, v) = (10, 10)$, $(u, v) = (8, 6)$, $(u, v) = (-8, 6)$, $(u, v) = (1, 10)$, and $(u, v) = (10, 1)$. The results show similar patterns of large bias errors in regions where $\mathbf{r}$ is poorly resolved. Therefore, if one interprets the OI estimates by mapping the uncertainty ellipses, then large and small ellipses may appear in the same location. Such discrepancies are an outcome of applying unidirectional flow fields where $\mathbf{r}$ may be only partially resolved. Generalizing, we next apply a varying flow field to study the source of uncertainties in the OI method.

b. *Multidirectional flow field*

1) DOUBLE-GYRE SYSTEM

We next examine a temporally and spatially varying flow field motivated by Shadden et al. (2005). This flow consists of a double-gyre system similar to the observed surface current patterns (Figs. 1, 5). We also incorporate a low-frequency time variation such that the flow field involves the two gyres propagating southward at ~0.3 m s^{-1} across the northeastern Chukchi Sea. The streamfunction for this test flow field is

$$\psi(x, y, t) = A \sin(K\pi f) \sin[K\pi(y - 71 + 0.02t)/4] + 3A \sin(10^{-4}\pi xy + t), \quad (11)$$

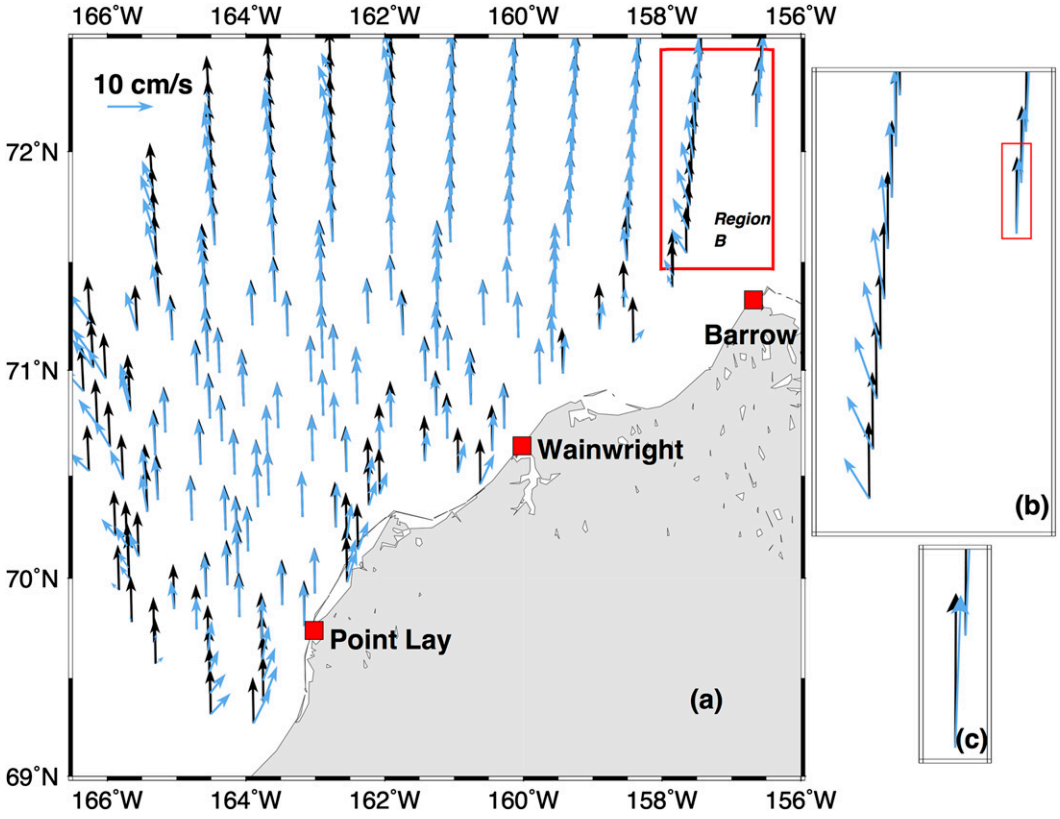

FIG. 7. (a) Example of the OI-estimated (blue) and UWLS-estimated (black) surface currents derived from modeled uniformly northward currents. OI and UWLS vectors are overlapped. For clarity, only subsampled vectors are shown. Red squares represent locations of HFR. Red rectangle highlights region B. (b) Enlargement of region B. (c) Enlargement to show the detail of the red rectangle area in (b).

where

$$f(x,t) = a[(x+169)/6.5)]^2 + b[(x+169)/6.5] \quad \text{and} \quad (12)$$

$$a(t) = E\sin(\omega t) \quad \text{and} \quad b(t) = 1 - 2E\sin(\omega t). \quad (13)$$

Parameters are t (an arbitrary integer), $E = 0.55$, $\omega = 2\pi/20$, $K = 1$ (scale factor), and $A = 50$. The velocity field $\mathbf{u}_m = (u_m, v_m)$ is then given by

$$u_m(x,y,t) = -\frac{\partial\psi}{\partial y} \quad \text{and} \quad v_m(x,y,t) = \frac{\partial\psi}{\partial x}. \quad (14)$$

Here u_m and v_m are computed for every grid point of $\mathbf{r}$ by (1) and then converted to their radial velocity components ($\mathbf{r}_m$). Note in the following analysis that these grid points mimic the coverage of the 2010 HFR observations and that the flagged locations indicated by the gaps in Fig. 3 have no data. The entire simulated velocity field lasts for 205 hourly time steps or ~8 days of HFR measurements. The $\mathbf{r}_m$ are used to estimate $\mathbf{u}$ using the OI method. We note that the estimated $\mathbf{u}$ are computed for an ideal situation insofar as the grid points of $\mathbf{r}_m$ for each of the three HFR have continuous data for the 205-h span, except for the flagged grid points. When modeled and OI-derived $\mathbf{u}$ are plotted together, disparities become evident (Fig. 8). In the regions farthest offshore, north of Icy Cape and in the HFR baselines, the resultant $\mathbf{u}$ differ in direction and magnitude. To examine the possibility that the OI method may oversmooth small-scale features, we also modeled a flow field having small-scale spatial variations by setting $K = 3$ in (11) (Fig. 8d). This small-scale flow field contains eddies of ~30-km radius in comparison to the test eddies with ~120-km radius. The results indicate that spatial variations on this scale are still captured by the OI technique.

2) STATISTICAL METRICS

The performance, or skill, of the OI method is based on quantitative agreement between the modeled ($\mathbf{u}_m$) and resulting currents ($\mathbf{u}$). Utilizing the test field described by (11)–(14) and following Willmott (1981), Warner et al. (2005), and Liu et al. (2010), the skill [on a (0–1) scale] is

$$\text{Skill} = \frac{1}{2}(\text{SU} + \text{SV}), \quad (15)$$

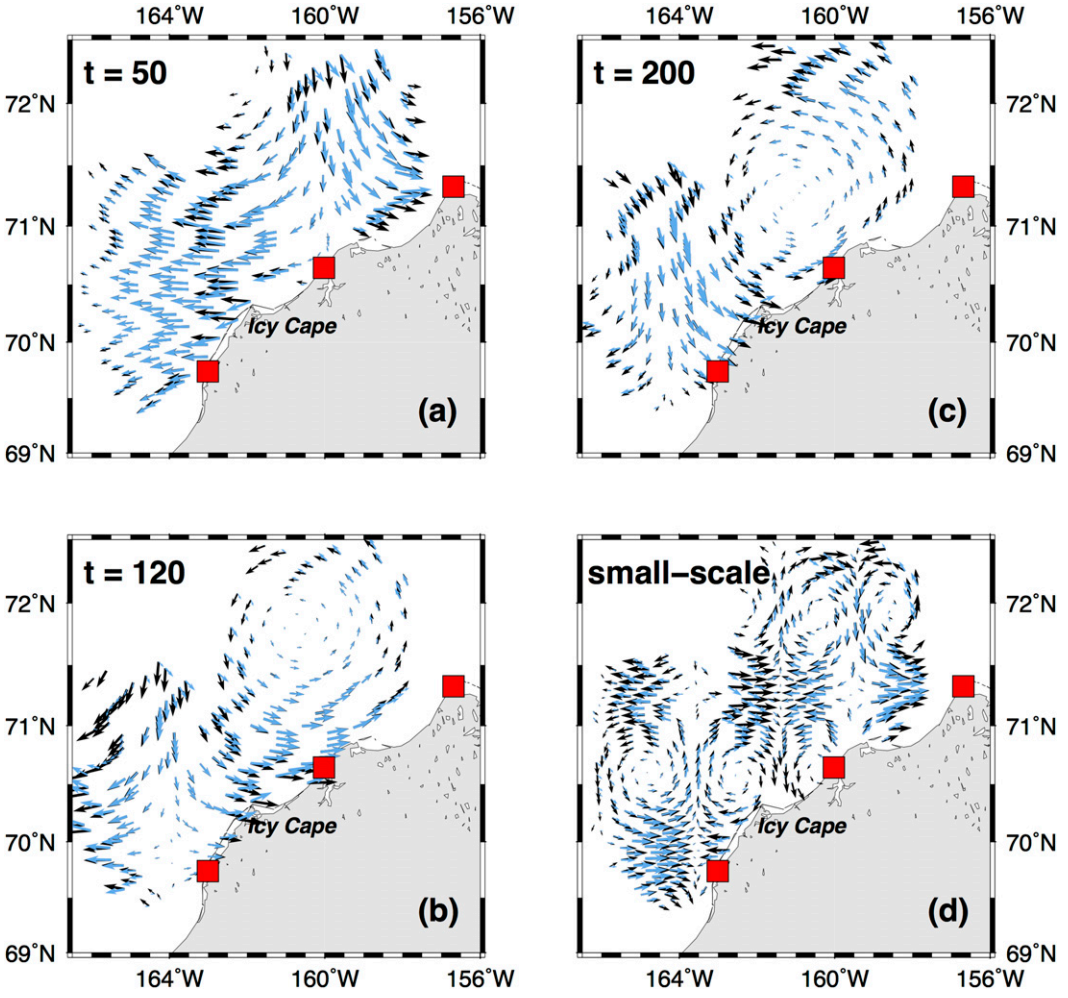

FIG. 8. (a)–(c) Modeled flow field based on (11)–(14) at three time steps. (d) An example of small-scale modeled flow field by changing the scale factor K from 1 to 3 in (11). Blue and black vectors are OI estimated and original modeled currents, respectively. OI and model vectors are overlapped. For clarity, only subsampled vectors are shown. Red squares represent locations of HFR.

where

$$\mathrm{SU} = 1 - \frac{\sum_{t=1}^{205} |u_{t,m} - u_{t,o}|^2}{\sum_{t=1}^{205} \left(|u_{t,m} - \overline{u}_{t,o}| + |u_{t,o} - \overline{u}_{t,o}|\right)^2} \quad \text{and} \quad (16)$$

$$\mathrm{SV} = 1 - \frac{\sum_{t=1}^{205} |v_{t,m} - v_{t,o}|^2}{\sum_{t=1}^{205} \left(|v_{t,m} - \overline{v}_{t,o}| + |v_{t,o} - \overline{v}_{t,o}|\right)^2}. \quad (17)$$

Subscripts m and o represent the modeled and the OI-estimated flow, respectively, and the overbar indicates an average of the 205 time steps. SU and SV represent the agreement between the known field and the OI estimate for the two velocity components. A skill = 1 indicates perfect agreement, and a skill = 0 indicates no agreement.

We also compute the complex correlation function for the two vector fields and the phase angle following (Kundu 1976; Shay et al. 2007)

$$\phi = \tan^{-1} \frac{\sum_{t=1}^{205} (u_{t,o} v_{t,m} - v_{t,o} u_{t,m})}{\sum_{t=1}^{205} (u_{t,o} u_{t,m} + v_{t,o} v_{t,m})}, \quad (18)$$

where ϕ is the average angular difference between the estimated vector and the modeled vector. A positive ϕ is the average cyclonic rotation of the modeled current with respect to the estimated current, and a negative ϕ is the average anticyclonic rotation.

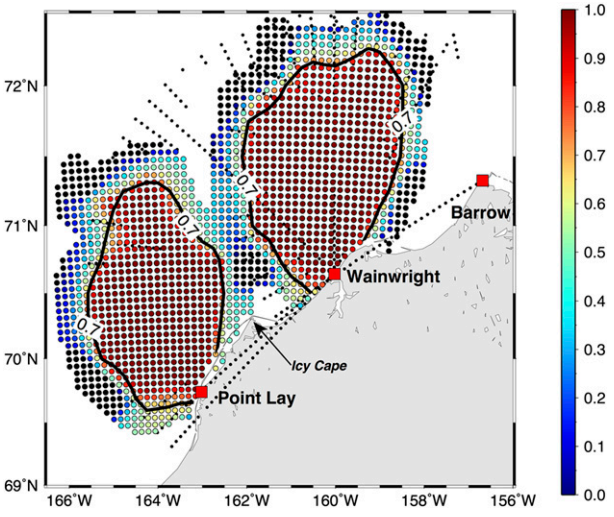

FIG. 9. Spatial distribution of skill (color shaded) of OI estimates. Small black dots indicate locations of quality flagged radial velocity measurements. Black contour denotes the 0.7 skill level. Red squares are the locations of HFR.

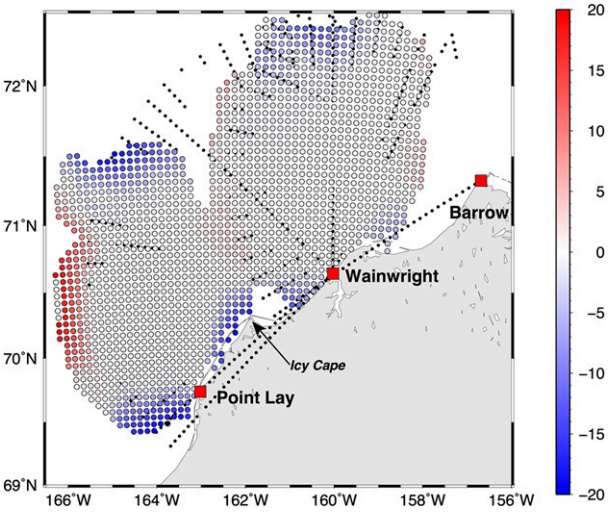

FIG. 10. Spatial distribution of phase shift (color shaded and in degrees) of OI estimates. Positive values mean counterclockwise rotation of the modeled current with respect to the OI-estimated current. Small black dots indicate locations of quality flagged radial velocity measurements. Red squares are the locations of HFR.

3) PERFORMANCE OF OI

The spatial distribution of the skill of the OI estimates (Fig. 9) shows areas of high confidence (skill ≥ 0.7). We chose a skill ≥ 0.7 as being reliable because the associated phase shifts, as discussed below, are also small. Of interest is that the skill in the gap north of Icy Cape is quite low (<0.4), suggesting that such areas cannot be reliably estimated by OI. Low-skill regions also circumscribe the high-skill interior. A majority of the low-skill regions coincide with the flagged grid points during the quality assurance/quality control (QA/QC) process (Fig. 3). This implies that these regions are incorporating relatively few **r** and/or that the **r** mostly originate from the same HFR site and thus yield large biases.

In the interior of the radar mask where the skill ≥ 0.7, phase shifts (Fig. 10) are quite small, ~2° (the difference in magnitude between the modeled and estimated vectors is <0.1%). However, phase shifts as large as 20° (accompanied by a reduction of ~6% in vector magnitude) occur along the baselines and the boundary of the radar mask. This result explains the weak currents and shear found in OI-estimated currents (Fig. 5). In summary, OI appears to be a robust estimator for a variable flow field in the interior of the radar mask although it is limited along the radar mask baselines and boundary.

4) FACTORS CONTROLLING OI PERFORMANCE

The number of available incorporating **r** (AR), within a 3-h averaging period, from all HFR in d_o is examined for every grid point of **u** (Fig. 11). The largest AR values are found near the HFR in Wainwright and Point Lay, and the lower AR values occur farther offshore from these HFR. When comparing Fig. 11 with Fig. 9, the area with high skill ($\geq$0.7) does not match that with high AR. If AR is the dominant factor influencing the skill of OI estimates, then Fig. 9 should have a distribution similar to the high AR distribution; however, higher AR values are found nearshore and decrease as one moves offshore—unlike skill, which remains high even in offshore regions, indicating that AR alone is not the sole factor influencing OI estimates.

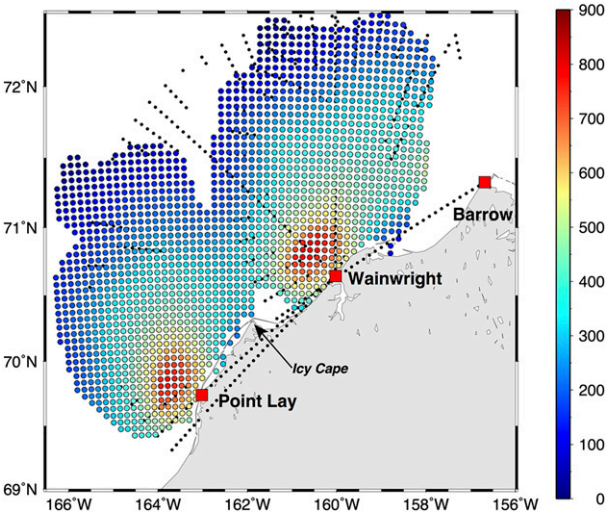

FIG. 11. Spatial distribution of AR (color shaded) for each OI grid point. Small black dots indicate locations of quality flagged radial velocity measurements. Red squares are the locations of HFR.

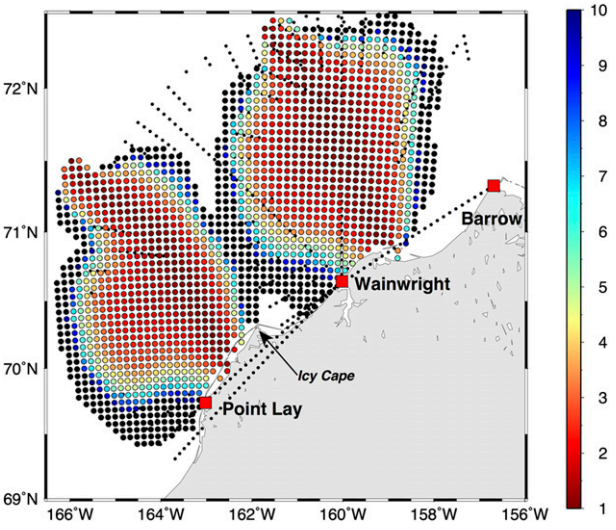

FIG. 12. Spatial distribution of ROR (color shaded) for each OI grid point. Small black dots indicate locations of quality flagged radial velocity measurements. Red squares are the locations of HFR.

In this regard, the number of **r** from each individual HFR plays an important role. We define the ratio of overlapping radial velocities (ROR) as

$$\mathrm{ROR}_{d_o} = \frac{\mathrm{NR}_1}{\mathrm{NR}_2}, \tag{19}$$

where NR_i, $i = 1, 2$ is the number of available incorporating **r** in d_o from each radar, with $i = 1$ and 2 being the primary and secondary **r** contributors, respectively. For example, for a 3-h averaging period for d_o at **x**, there are 60 **r** from Wainwright, 20 from Barrow, and 15 from Point Lay, then ROR at **x** is 60/20 = 3. ROR is related to geometric radial coverage and, ideally, it should be close to 1. An ROR much greater than one means the incorporating **r** are primarily from one radar site. ROR is useful in ascertaining potential bias errors, which can be represented by the contribution of available incorporating **r** in d_o. For cases where $i > 2$, we argue that the role of the ith HFR is insignificant here, but it can be beneficial to condition $\mathbf{cov}_{dm}^{\mathrm{T}}\,\mathbf{cov}_{dd}^{-1}$ as discussed below.

The spatial distribution of ROR at each grid point is shown in Fig. 12. Two regions with relatively low ROR (<4) are encircled by areas with high ROR (>7), similar to the spatial distribution of skill (i.e., regions with high ROR correspond with locations of low-skill OI estimates). This suggests that ROR is more important than AR in the OI method and that it helps to explain the discrepancies in the unidirectional flow cases. ROR is high in regions where **r** is predominantly from a single radar site and high bias errors are found. Consequently, near the observation gap north of Icy Cape, where AR has a modest value (~400), the skill is low and does not necessarily correspond to the AR score. Regions with low ROR tend to be properly resolved with reduced bias errors, suggesting ROR is a better proxy than AR for interpreting data quality.

It is interesting to examine the response of OI estimates in areas with low AR and low ROR. Although low ROR appears to provide a better index of data quality, the fundamental basis of OI is the correlation function (10). If the correlation function fails to describe the relationship between **r** in circumstances when AR and ROR are low, then the correlation function will be poorly represented in (8) and (9). Since this function is used in forming the linear estimates of **u** based on **r** by (2), we need to understand the sensitivity of the OI method to the correlation structure, which depends upon AR and ROR.

OI is a linear estimation method, in which $\mathbf{cov}_{dm}^{\mathrm{T}}\,\mathbf{cov}_{dd}^{-1}$ is the mathematical operator that estimates **u** from **r**. In objective analysis, $\mathbf{cov}_{dm}^{\mathrm{T}}\,\mathbf{cov}_{dd}^{-1}$ represents the correlation matrix in which the positive definiteness is described by fitting an analytical correlation function (10). If the current field is difficult to describe analytically, then correlation estimates that do not yield positive definite matrices will be sensitive to small variations in the analysis parameters and can result in erratic estimates (Carter and Robinson 1987). This sensitivity can be measured by computing the CN of the correlation matrix, indicating how much the error is magnified upon converting **r** to **u** (Arfken et al. 2005). Even small variations in **r** may lead to large changes in **u** if CN is large. Recall that CN results from the matrix containing both angles and the correlation function, whereas GDOP is solely from the angle matrix. Hence, as mentioned in section 3, we suggest that CN is the OI analog to GDOP, preferred in the UWLS method.

We computed the CN of $\mathbf{cov}_{dm}^{\mathrm{T}}\,\mathbf{cov}_{dd}^{-1}$ and plotted its spatial distribution at each grid point for which there is a corresponding OI estimate (Fig. 13). Grid points with relatively high CN (>5) encircle the outer edge of the radar mask and those with low CN (<2) (centered around 70.5°N, 164°W and 71.5°N, 160°W) are similar to the spatial distribution of skill (>0.7) and phase shift (<2°) (Figs. 9, 10). A comparison of the CN map with the ROR pattern indicates that high CN areas match areas with high ROR. When we encounter regions of low CN that coincide with high ROR, the skill may be low, indicating that while $\mathbf{cov}_{dm}^{\mathrm{T}}\,\mathbf{cov}_{dd}^{-1}$ may be well conditioned, the estimator is dependent on the contribution of the incorporating **r**.

The spatial patterns of AR, ROR, and CN suggest a relationship among these factors. The correlation between ROR versus AR is −0.01 and not significantly

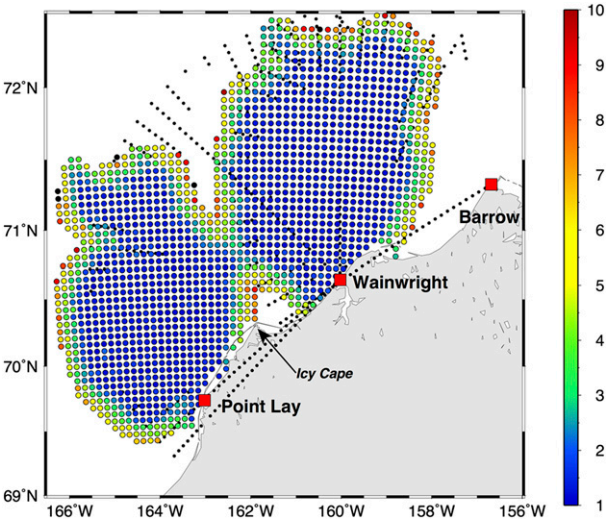

FIG. 13. Spatial distribution of CN (color shaded) of $\mathbf{cov}_{dm}^{\mathrm{T}}\,\mathbf{cov}_{dd}^{-1}$ at each grid point of the OI estimates. Small black dots indicate locations of quality flagged radial velocity measurements. Red squares are the locations of HFR.

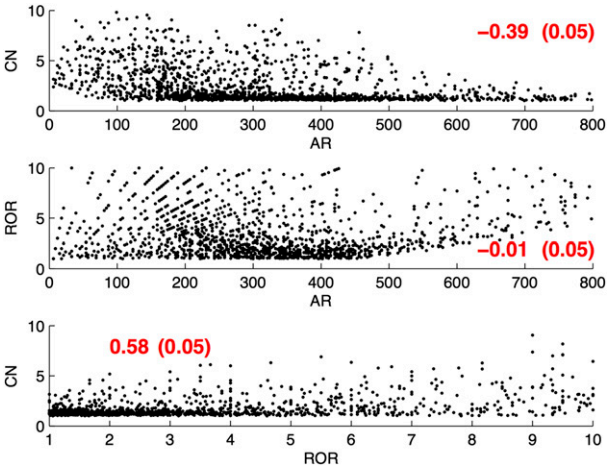

FIG. 14. Scatterplots of (top) CN vs AR, (middle) ROR vs AR, and (bottom) CN vs ROR for the double-gyre system (see Figs. 11–13). Corresponding correlation coefficient is shown in red, and number in parenthesis refers to the 95% significant level. Note the x and y axes have different scales.

different from 0. However, the correlation between CN and AR is −0.39 and that between CN and ROR is 0.58, with both results significant at the 95% level (Fig. 14). Therefore, CN is a function of both AR and ROR. In most HFR operations, data gaps are unavoidable and, as gaps occur, the AR and ROR patterns will change, modifying the structure of the correlation matrix and affecting current estimates. Our analysis shows that AR, ROR, and CN interact with each other during data processing and affect the accuracy of OI estimates.

AR is based on the HFR data, while CN is based on the correlation matrix. However, prior to HFR setup and operation, these two factors are unknown. ROR is a result of the radar geometry due to HFR siting, which can be examined beforehand. Once d_o is decided, the ROR pattern can be determined for the OI-estimated currents. This may be crucial for site planning or short-term deployments of HFR (Barrick et al. 2012). Thus, we suggest that ROR serve as a planning tool in assessing potential errors in OI.

5) SENSITIVITIES TO RANDOM GAPS

The previous analysis is based on noise- and gap-free conditions, which is not realistic in most HFR operations. Kim et al. (2008) show that the OI method can effectively smooth noise and provide more precise solutions than the UWLS method, true for Gauss–Markov estimators (Wunsch 2006). Kim et al. (2008) did not examine the sensitivity of OI to data with temporal gaps. We consider a simple condition in which the signal-to-noise ratio of the returned radar signal is below 6 dB (the default threshold in SeaSonde processing software). In this case, the spectra will be flagged as an outlier and produce a gap in **r**. The following effort seeks to understand the consequences of observation gaps on the quality of OI estimates.

We apply the Monte Carlo method on nine selected grid points (Fig. 15) chosen to represent areas in the interior (IS, IN), edge (ESW, ENW, ENE1, ENE2, EN), and central (C1, C2) portions of the radar mask. To derive statistically independent comparisons, the d_o for each of the chosen grid points do not overlap. Using the double-gyre flow field, 10%–90% of the grid points in d_o are randomly assigned as gaps for all time steps. Note that the remaining **r** are still noise free. We then form skill estimates following (15)–(17), with this procedure repeated 100 times to form 95% confidence intervals on the estimated mean. The presence of gaps also means that the structure of $\mathbf{cov}_{dm}^{\mathrm{T}}\,\mathbf{cov}_{dd}^{-1}$ may be changed, so we compute the CN after each iteration.

Variation in the skill of OI estimates and the CN of $\mathbf{cov}_{dm}^{\mathrm{T}}\,\mathbf{cov}_{dd}^{-1}$ are shown in Fig. 16. The interior grid points (IS, IN) are very resilient to gaps, even when only 10% of the data occurs in the d_o. This result further underscores the importance of high AR and low ROR, for it enables **u** in regions with densely overlapping **r** to be well resolved. It also suggests that velocity estimates can be properly resolved based on a priori statistics even though there may be many data gaps in such regions. For grid points initially having low skill in the gap-free simulations (e.g., ESW, C2, ENE1, ENE2, and EN), adding gaps further erodes the skill. When gaps of 60% or more occur in d_o, the skill values are all below 0.2 in

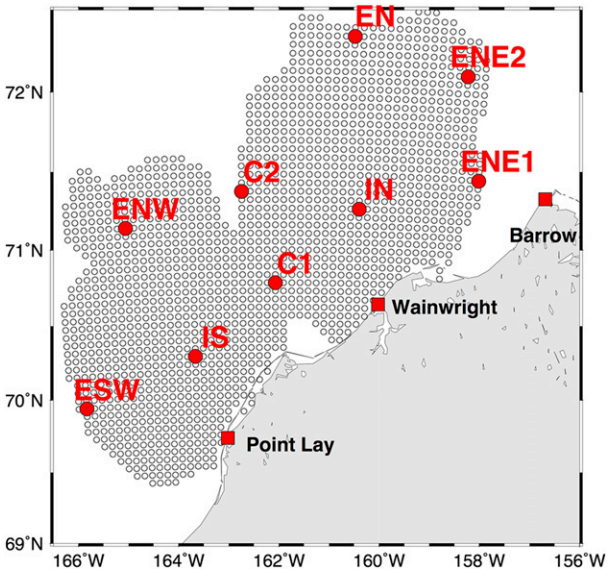

FIG. 15. Gray circles are grid points for OI estimates. Red dots, enlarged for clarity, indicate locations of grid points for the gap sensitivity experiment. Red squares are the locations of HFR.

areas with low AR and high ROR. Therefore, increasing the number of gaps in these regions implies that the available **r** tends to originate from the same HFR site and results in bias. For example for ENW, the skill drops substantially as the number of gaps increases. Consequently, in cases where there are random gaps, high AR and low ROR are required for reliable OI estimates. This result also highlights that site spacing of the HFR array plays an important role in estimating surface currents using the OI method. If the spacing between HFR sites is not optimal, then better data coverage can be improved using the OI method, but in certain regions it may introduce significant bias errors into the resulting current estimates.

5. Discussion and summary

We have assessed the performance of the OI method on an HFR dataset from the Chukchi Sea with site spacing farther than optimal. The focus of the study was on the feasibility of OI under these circumstances and to investigate the applicability of the OI method. Our results offer suggestions and a simple tool to diagnose the performance of the OI method for the broader HFR community. Three factors influence the OI-derived data quality: 1) the number of available incorporating **r** (AR) for calculating **u**; 2) the ratio of the incorporating **r** from overlapping HFR sites used in calculating **u** (ROR or radar geometry); and 3) the positive definiteness [condition number (CN)] of the correlation matrix can be regarded as the equivalent to GDOP for UWLS. For operational purposes, the potential performance of the OI method can

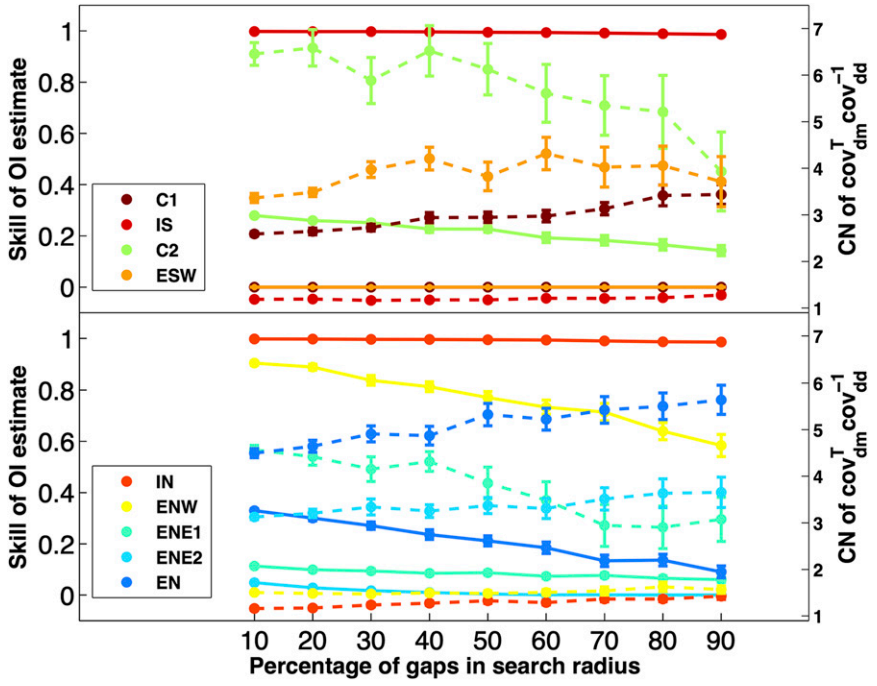

FIG. 16. Variation in OI estimate skill (solid lines) and the condition number of $\mathbf{cov}_{dm}^{T}\mathbf{cov}_{dd}^{-1}$ (dashed lines) for varying gap percentages in the search radius. Vertical bars indicate the 95% confidence interval. Note that the skill lines for C1 and ESW are overlapped.

be evaluated by examining ROR patterns and it may be of value in choosing HFR sites. Our idealized experiments show that the OI method is a robust technique in dealing with flow variability and that it provides current estimates with smaller variance than the conventional UWLS method. Regions within the radar mask with high AR and low ROR **u** can be reliably constructed with the OI method even though there may be gaps in the radial data. However, careful attention needs to be paid if the AR is limited because this may result in a high CN and an ill-conditioned correlation matrix, which will amplify errors. If the incorporating **r** are mainly contributed by a single radar site (high ROR), significant bias errors can arise.

This study does not take into account the influence of random noise, which can be widespread and sporadic, although one common situation considered here is the diurnal interference of the ionosphere. Since this interference is widespread, we have conducted Monte Carlo experiments by adding random noise with varying magnitude on each **r** in d_o. The result (not shown) indicates that the skill of the OI estimates drops as the magnitude of noise increases. A similar pattern is found if **u** are estimated through the UWLS method. Therefore, if the noise source is widespread and comparable to the signal strength, then both the UWLS and OI methods lose the ability to make accurate estimates.

The main departure of the OI method from the UWLS method is the use of larger d_o and weighted radials to produce smoother currents and greater data coverage in the resultant current map. We find the major source of erroneous estimates using the OI method depends on ROR, which is a direct function of HFR siting. Before applying the OI method to HFR data, we recommend an analytical flow field (such as that described in section 4) with multidirectional patterns to create a map of estimated skill, as this will assist in identifying regions of possible erroneous estimates. Conveniently, ROR can be computed before site installation to highlight locations of substantial bias errors. ROR can also be computed in real-time data processing, to provide a tracking criterion for how bias errors may be introduced into the OI surface current estimates.

Acknowledgments. We very much appreciate the assistance of Dr. Sung Yong Kim, who provided the OI algorithm for analysis. We also thank the Barrow Arctic Science Consortium for the logistical support; the Ukpeaġvik Iñupiat Corporation, the Olgoonik Corporation, and the Cully Corporation for the use of their lands; and the villages of Barrow, Wainwright, and Point Lay Alaska for their cooperation and support. Data collection was supported by BOEM Contract M09AC15207, Conoco Phillips, Inc., and Shell Exploration and Production Company. Data analysis was supported by BOEM Contract M12AC000008.

REFERENCES

Arfken, G. B., H. Weber, and F. Harris, 2005: *Mathematical Methods for Physicists.* 6th ed. Elsevier Academic Press, 1200 pp.

Barrick, D., 2006: Geometrical dilution of statistical accuracy (GDOSA) in multi-static HF radar networks. CODAR Ocean Sensors Rep., 9 pp. [Available online at http://www.codar.com/images/about/2006Barrick_GDOSA.pdf.]

——, and B. Lipa, 1986: Correcting for distorted antenna patterns in CODAR ocean surface measurements. *IEEE J. Oceanic Eng.,* **11,** 304–309, doi:10.1109/JOE.1986.1145158.

——, V. Fernandez, M. I. Ferrer, C. Whelan, and Ø. Breivik, 2012: A short-term predictive system for surface currents from a rapidly deployed coastal HF radar network. *Ocean Dyn.,* **62,** 725–740, doi:10.1007/s10236-012-0521-0.

Carter, E. F., and A. R. Robinson, 1987: Analysis models for the estimation of oceanic fields. *J. Atmos. Oceanic Technol.,* **4,** 49–74, doi:10.1175/1520-0426(1987)004<0049:AMFTEO>2.0.CO;2.

Chapman, R. D., L. K. Shay, H. C. Graber, J. B. Edson, A. Karachintsev, C. L. Trump, and D. B. Ross, 1997: On the accuracy of HF radar surface current measurements: Intercomparisons with ship-based sensors. *J. Geophys. Res.,* **102,** 18 737–18 748, doi:10.1029/97JC00049.

Crombie, D. D., 1955: Doppler spectrum of sea echo at 13.56 Mc./s. *Nature,* **175,** 681–682, doi:10.1038/175681a0.

Fang, Y. C., J. Wang, Y. J. Yang., J. C. Mau, K. H. Thia, and M. J. Huang, 2011: Preliminary results of CODAR surface current observations northeast of Taiwan. *Proc. 2011 Int. Workshop on Operating System for Marine Environment Monitoring and Forecasting,* Kaohsiung, Taiwan, National Kaohsiung Marine University, 59–77.

Gurgel, K.-W., 1994: Shipborne measurement of surface current fields by HF radar. *OCEANS'94: Oceans Engineering for Today's Technology and Tomorrow's Preservation; Proceedings,* P. Sabathé, Ed., Vol. 3, IEEE, III/23–III/27.

Kim, S. Y., E. Terrill, and B. Cornuelle, 2007: Objectively mapping HF radar-derived surface current data using measured and idealized data covariance matrices. *J. Geophys. Res.,* **112,** C06021, doi:10.1029/2006JC003756.

——, E. J. Terrill, and B. D. Cornuelle, 2008: Mapping surface currents from HF radar radial velocity measurements using optimal interpolation. *J. Geophys. Res.,* **113,** C10023, doi:10.1029/2007JC004244.

Kohut, J., H. Roarty, E. Randall-Goodwin, S. Glenn, and C. S. Lichtenwalner, 2012: Evaluation of two algorithms for a network of coastal HF radars in the Mid-Atlantic Bight. *Ocean Dyn.,* **62,** 953–968, doi:10.1007/s10236-012-0533-9.

Kundu, P. K., 1976: Ekman veering observed near the ocean bottom. *J. Phys. Oceanogr.,* **6,** 238–242, doi:10.1175/1520-0485(1976)006<0238:EVONTO>2.0.CO;2.

Lipa, B., 2003: Uncertainties in SeaSonde current velocities. *Proceedings of the IEE/OES Seventh Working Conference on Current Measurement Technology,* J. A. Rizoli, Ed., IEEE, 95–100.

——, and D. Barrick, 1983: Least-squares methods for the extraction of surface currents from CODAR crossed-loop data: Application at ARSLOE. *IEEE J. Oceanic Eng.,* **8,** 226–253, doi:10.1109/JOE.1983.1145578.

Liu, Y., R. H. Weisberg, C. R. Merz, S. Lichtenwalner, and G. J. Kirkpatrick, 2010: HF radar performance in a low-energy

environment: CODAR SeaSonde experience on the West Florida shelf. *J. Atmos. Oceanic Technol.,* **27,** 1689–1710, doi:10.1175/2010JTECHO720.1.

Paquette, R. G., and R. H. Bourke, 1974: Observations on the coastal current of arctic Alaska. *J. Mar. Res.,* **32,** 195–207.

Shadden, S. C., F. Lekien, and J. E. Marsden, 2005: Definition and properties of Lagrangian coherent structures from finite-time Lyapunov exponents in two-dimensional aperiodic flows. *Physica D,* **212,** 271–304, doi:10.1016/j.physd.2005.10.007.

Shay, L. K., J. Martinez-Pedraja, T. M. Cook, B. K. Haus, and R. H. Weisberg, 2007: High-frequency radar mapping of surface currents using WERA. *J. Atmos. Oceanic Technol.,* **24,** 484–503, doi:10.1175/JTECH1985.1.

Stewart, R. H., and J. W. Joy, 1974: HF radio measurements of surface currents. *Deep-Sea Res. Oceanogr. Abstr.,* **21,** 1039–1049, doi:10.1016/0011-7471(74)90066-7.

Teague, C., 2001: Ionospheric effects on coastal radar systems. *Radiowave Oceanography: The First International Workshop,* H. C. Graber and J. D. Paduan, Eds., University of Miami, 56–61.

Warner, J. C., W. R. Geyer, and J. A. Lerczak, 2005: Numerical modeling of an estuary: A comprehensive skill assessment. *J. Geophys. Res.,* **110,** C05001, doi:10.1029/2004JC002691.

Weingartner, T., S. Danielson, Y. Sasaki, V. Pavlov, and M. Kulakov, 1999: The Siberian Coastal Current: A wind- and buoyancy-forced Arctic coastal current. *J. Geophys. Res.,* **104,** 29 697–29 713, doi:10.1029/1999JC900161.

——, K. Aagaard, R. Woodgate, S. Danielson, Y. Sasaki, and D. Cavalieri, 2005: Circulation on the north central Chukchi Sea shelf. *Deep-Sea Res. II,* **52,** 3150–3174, doi:10.1016/j.dsr2.2005.10.015.

——, P. Winsor, R. A. Potter, H. Statscewich, and E. L. Dobbins, 2013: Application of high frequency radar to potential hydrocarbon development areas in the northeast Chukchi Sea. Final Rep., U.S. Dept. of the Interior, Alaska Outer Continental Shelf Region Contract M09AC15207, OCS Study BOEM 2012-079, 162 pp. [Available online at www.data.boem.gov/PI/PDFImages/ESPIS/5/5266.pdf.]

Willmott, C. J., 1981: On the validation of models. *Phys. Geogr.,* **2,** 184–194, doi:10.1080/02723646.1981.10642213.

Winsor, P., and D. C. Chapman, 2004: Pathways of Pacific water across the Chukchi Sea: A numerical model study. *J. Geophys. Res.,* **109,** C03002, doi:10.1029/2003JC001962.

Wunsch, C., 2006: *Discrete Inverse and State Estimation Problems: With Geophysical Fluid Applications.* Cambridge University Press, 371 pp.